

Path-Decoupled Hyperbolic Flow Matching for Few-Shot Adaptation

Lin Li¹ Ziqi Jiang¹ Gefan Ye² Zhenqi He¹ Jiahui Li² Jun Xiao² Kwang-Ting Cheng¹ Long Chen¹

Abstract

Recent advances in cross-modal few-shot adaptation treat visual-semantic alignment as a continuous feature transport problem via Flow Matching (FM). However, we argue that Euclidean-based FM overlooks fundamental limitations of flat geometry, where polynomial volume growth fails to accommodate diverse feature distributions, leading to severe **path entanglement**. To this end, we propose path-decoupled Hyperbolic Flow Matching (HFM), leveraging the Lorentz manifold’s exponential expansion for trajectory decoupling. HFM structures the transport via two key designs: 1) *Centripetal hyperbolic alignment*: It constructs a centripetal hierarchy by anchoring textual roots, which pushes visual leaves to the boundary to initialize orderly flows. 2) *Path-decoupled objective*: It acts as a “semantic guardrail” rigidly confining trajectories within isolated class-specific geodesic corridors via step-wise supervision. Furthermore, we devise an adaptive *diameter-based stopping* to prevent over-transportation into the crowded origin based on the intrinsic semantic scale. Extensive ablations on 11 benchmarks have shown that HFM establishes a new state-of-the-art, consistently outperforming its Euclidean counterparts. Our codes and models will be released.

1. Introduction

The remarkable zero-shot generalization of pretrained vision-language models (VLMs), such as CLIP (Radford et al., 2021), builds upon their ability to embed images and natural language into a shared semantic embedding space (Jia et al., 2021; Li et al., 2022; Zhong et al., 2022). Although such joint representations facilitate zero-shot classification via cross-modal similarity, a large performance gap remains when encountering specialized downstream tasks (Zhou et al., 2022b; Zhang et al., 2022). To bridge

¹The Hong Kong University of Science and Technology (HKUST) ²Zhejiang University. Correspondence to: Long Chen <longchen@ust.hk>.

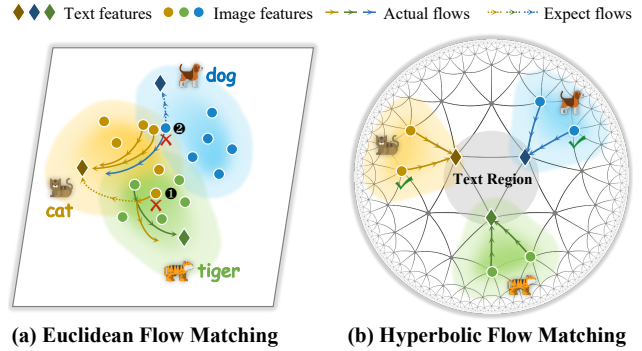


Figure 1. Illustration of Path Entanglement. (a) Euclidean Flow Matching suffers from severe trajectory collisions (e.g., “cat” intersecting “tiger” and “dog” merging with “cat”) due to the limited polynomial capacity of flat geometry. (b) Hyperbolic Flow Matching uses exponential volume expansion to achieve path decoupling.

this gap, few-shot adaptation (Zhou et al., 2022b;a; Zhang et al., 2022; Gao et al., 2024) aims to refine the pre-trained encoders, leveraging minimal supervisory signals to realign visual features with their corresponding textual prototypes.

To achieve such adaptation, various Parameter-Efficient Fine-Tuning (PEFT) techniques, e.g., prompt tuning (Zhou et al., 2022b;a) and feature-level adapters (Gao et al., 2024; Hu et al., 2022a; Zanella & Ben Ayed, 2024), have been widely adopted to refine latent representations. However, these methods predominantly rely on a “one-step” adjustment, where the alignment is restricted to a single forward pass of the adapter module. Such a direct transformation often struggles to resolve complex semantic entanglements in challenging datasets, due to the lack of the iterative rectification inherent in continuous processes (Jiang et al., 2025). To address this, recent efforts like FMA (Jiang et al., 2025) treat alignment as a continuous feature transport problem via Flow Matching (FM) (Lipman et al., 2022; Liu et al., 2022) strategy. Specifically, they construct conditional flow paths that guide visual features from the image manifold to the corresponding class-specific text regions, thereby eliminating the cross-modal gap for classification. By learning a velocity field that defines a time-continuous evolution, the aforementioned methods enable multi-step rectification. This iterative refinement allows the model to progressively correct alignment errors, enabling superior expressive capacity over one-step counterparts.

Despite the theoretical flexibility of multi-step flows, we

argue that existing Euclidean FM models suffer from severe inherent **path entanglement**. It refers to the transport paths that inadvertently intersect, overlap, or merge within the latent space. Fundamentally, this entanglement arises because the polynomial volume growth of flat geometry fails to accommodate diverse feature distributions, leading to two inevitable structural interferences: ❶ **Disordered Cross-Modality Flows**. Source image features and their corresponding target semantic prototype are embedded in *irregularly dispersed* positions. Bridging this unstructured gap necessitates long-range transport, thereby increasing the risk of trajectory collisions (*e.g.*, the yellow flow of the “cat” colliding with and following the green path of the “tiger” in Figure 1a). This chaotic confluence erodes feature discriminability, thereby compromising the classification performance. ❷ **Crowded Inter-Class Flows**. Flow sources from different categories may unintentionally overlap, leading to more ambiguous transport trajectories. Without sufficient separation, these paths are easily diverted by *high-density neighboring clusters* (*e.g.*, the blue flow of “dog” drifting into the dense yellow samples in Figure 1a).

To this end, in this paper, we propose a new path-decoupled **Hyperbolic Flow Matching (HFM)** for few-shot adaptation. By reformulating the transport dynamics within the Lorentz manifold, we exploit the exponential volume growth of hyperbolic geometry to spatially decouple the transport trajectories to alleviate path entanglement. To address ❶, we employ a mechanism of **centripetal hyperbolic alignment**. It restructures the latent geometry into a concentric hierarchy by explicitly initializing textual prototypes with small hyperbolic radii (proximal to the origin, visualized as the central “Text Region” in Figure 1b) and visual features near the manifold boundary. To enforce this *centripetal order*, we leverage the *cross-modality entailment* objective (Desai et al., 2023) to optimize the embedding space, formally establishing text as the semantic root and images as entailment leaves. By constraining centripetal order flows to focusing radial geodesics, we can reduce trajectory collisions, thereby preserving semantic discriminability and enhancing classification performance. To tackle ❷, we introduce a **path-decoupled objective**. Leveraging the exponential volume expansion near the manifold boundary, this objective maximizes the geodesic margin between distinct semantic categories. This optimization explicitly constructs isolated geodesic transport corridors (illustrated as the separated yellow, green, and blue areas in Figure 1b), ensuring that each class-specific flow evolves within a unique, non-overlapping volume. Consequently, this geometric separation effectively decouples inter-class trajectories, preventing the ambiguous overlaps inherent to crowded Euclidean spaces.

Furthermore, in the inference stage, to enhance inference efficiency and accuracy, we devise an adaptive **diameter-based stopping** strategy. By dynamically terminating the

flow upon the convergence of geometric compactness, we prevent over-transportation into the densely populated text region near the origin. This avoids the critical risk of visual features drifting into adjacent, incorrect clusters due to spatial crowding, ensuring both precise classification and minimal computational overhead.

Extensive experiments on 11 few-shot benchmarks demonstrate that our HFM consistently surpasses state-of-the-art Euclidean-based FM counterparts and PEFT adapters as a plug-and-play module. These promising results evidence the significant potential of non-Euclidean manifolds for advancing the frontier of few-shot cross-modal understanding.

2. Related Works

Few-shot Adaptions in VLMs. Few-shot adaptation is a task that requires models to learn from only a few annotated examples (Chen et al., 2020; Hou et al., 2019; Wang et al., 2020). Current approaches in VLMs usually follow the paradigm that employs pre-trained VLMs and then refines them through task-adaptive optimization. Parameter-Efficient Fine-Tuning (PEFT) (Gu et al., 2022; Hu et al., 2023; Lee et al., 2023; Zhang et al., 2022; Zanella & Ben Ayed, 2024; De Marinis et al., 2025) is one of popular optimization methods, which focuses on updating a small subset of parameters to achieve performance comparable to full fine-tuning. In the meanwhile, some studies explore the potential of in-context learning (Alayrac et al., 2022; Zhang et al., 2023; Hu et al., 2022b; Cai et al., 2023; Huang et al., 2024) in few-shot adaptation. With no change on model parameters, they add support examples into the inference context to make pre-trained models adapt to specific tasks. Despite computational efficiency and effectiveness, their one-step adjustment fails to disentangle complex feature distributions, leaving substantial room for improvement.

Hyperbolic Representation Learning. Hyperbolic geometry, such as Poincaré-ball Model (Nickel & Kiela, 2017) and Lorentz Model (Nickel & Kiela, 2018), demonstrates extraordinary capability in modeling hierarchical relationships due to its exponential volume growth relative to radius. With custom-designed neural network modules (Chen et al., 2022b; Liu et al., 2019; Li et al., 2025c), hyperbolic representation learning has achieved profound breakthroughs in a wide range of tasks in different modalities, including text (Dhingra et al., 2018; Zhu et al., 2020; Le et al., 2019), image (Atigh et al., 2022; Khulkov et al., 2020; Li et al., 2023), audio (Petermann et al., 2023; Nakashima et al., 2022) and video (Li et al., 2025b;a). Meanwhile, combining with contrastive learning methods enables hyperbolic representation learning to successfully adapt to cross-modal tasks (Wen et al., 2025; Desai et al., 2023; Liu et al., 2020; Hong et al., 2023). Given the inherent cross-modality hierarchy of the data in few-shot adaptation task, we try to harness

the power of hyperbolic geometry for flow matching.

Flow Matching (FM). Diffusion Model (Ho et al., 2020; Song et al., 2020; Rombach et al., 2022) is a powerful generative tool, but limited by slow inference due to curved sampling paths. Flow Matching (Lipman et al., 2022; Liu et al., 2022) addresses this limitation by learning vector fields that generate straight-line trajectories between distributions. Specifically, the utilization of optimal transport simplifies the geometric structure of the vector field, thus facilitating faster and more accurate sampling. From the perspective of stochastic interpolants, FM and diffusion models act as special cases within a unifying framework (Albergo et al., 2023). In spite of remarkable successes in domains like image generation (Ren et al., 2024; Esser et al., 2024; Luo et al., 2025), FM has recently been introduced to cross-modal adaptation. Notable works like FMA (Jiang et al., 2025) treat visual-semantic alignment as a continuous feature transport problem. However, constrained by flat geometry, these Euclidean-based FM often suffer from path entanglement, impairing the classification performance.

3. Approach

In this section, we present HFM, a path-decoupled framework designed to alleviate the path entanglement in few-shot adaptation. As illustrated in Figure 2, our HFM comprises three phases: 1) **Constructing Centripetal Hyperbolic Space** (§3.2): Establishing a centripetal hierarchy by anchoring textual roots at the origin and visual leaves at the boundary. 2) **Learning Path-Decoupled Flows** (§3.3): Optimizing a tangent velocity field to confine transport within isolated geodesic corridors via step-wise and contrastive supervision. 3) **Inference with Diameter-based Stopping** (§3.4): Employing a density-aware termination criterion to prevent over-transportation in crowded text region.

3.1. Preliminaries: Lorentz Model

We first briefly introduce the key concepts of hyperbolic geometry on which our HFM relies. Following (Desai et al., 2023; Pal et al., 2025), we adopt the Lorentz model of hyperbolic space $\mathbb{L}^{n,\kappa}$ with *learnable* constant negative curvature $-\kappa$ ($\kappa > 0$). In this model, each point $\mathbf{x} \in \mathbb{L}^{n,\kappa}$ consists of a time-like scalar x_0 and a space-like vector $\tilde{\mathbf{x}}$, constrained by the geometric property $\langle \mathbf{x}, \mathbf{x} \rangle_{\mathbb{L}} = -1/\kappa$. The Lorentzian inner product is formulated as $\langle \mathbf{x}, \mathbf{y} \rangle_{\mathbb{L}} = -x_0 y_0 + \langle \tilde{\mathbf{x}}, \tilde{\mathbf{y}} \rangle_{\mathbb{E}}$, where $\langle \cdot, \cdot \rangle_{\mathbb{E}}$ is the Euclidean inner product.

Geodesics. The shortest path between two points on the manifold, written as $d_{\mathbb{L}}(\mathbf{x}, \mathbf{y}) = \frac{1}{\sqrt{\kappa}} \operatorname{arccosh}(-\kappa \langle \mathbf{x}, \mathbf{y} \rangle_{\mathbb{L}})$.

Tangent and Manifold Projection. To map Euclidean features from CLIP into $\mathbb{L}^{n,\kappa}$, we employ the *exponential map* (Nickel & Kiela, 2018) defined at the tangent space of a reference point \mathbf{z} . To align with this geometry, the

original Euclidean feature $\tilde{\mathbf{x}}_{\mathbb{E}} \in \mathbb{R}^n$ is lifted into the $(n+1)$ -dimensional ambient tangent space $T_{\mathbf{z}}\mathbb{L}$, satisfying the orthogonality constraint with \mathbf{z} . Consequently, the projection onto the manifold to obtain $\mathbf{x} \in \mathbb{L}^{n,\kappa}$ is formulated as:

$$\mathbf{x} = \exp_{\mathbf{z}}^{\kappa}(\mathbf{x}_{\mathbb{E}}) = \cosh(\sqrt{\kappa}\|\mathbf{x}_{\mathbb{E}}\|_{\mathbb{L}})\mathbf{z} + \frac{\sinh(\sqrt{\kappa}\|\mathbf{x}_{\mathbb{E}}\|_{\mathbb{L}})}{\sqrt{\kappa}\|\mathbf{x}_{\mathbb{E}}\|_{\mathbb{L}}}\mathbf{x}_{\mathbb{E}}, \quad (1)$$

where $\mathbf{x}_{\mathbb{E}}$ refers to the lifted ambient vector derived from $\tilde{\mathbf{x}}_{\mathbb{E}}$. Conversely, the *logarithmic map* serves as the inverse operation, projecting a point \mathbf{x} from the manifold back to the tangent space at \mathbf{z} to recover the Euclidean features:

$$\mathbf{x}_{\mathbb{E}} = \log_{\mathbf{z}}^{\kappa}(\mathbf{x}) = \frac{\operatorname{arccosh}(-\kappa\langle \mathbf{z}, \mathbf{x} \rangle_{\mathbb{L}})}{\sqrt{\langle \mathbf{z}, \mathbf{x} \rangle_{\mathbb{L}}^2 - 1/\kappa^2}} \Pi_{T_{\mathbf{z}}\mathbb{L}}(\mathbf{x}), \quad (2)$$

where $\Pi_{T_{\mathbf{z}}\mathbb{L}}(\mathbf{x}) = \mathbf{x} + \kappa\langle \mathbf{z}, \mathbf{x} \rangle_{\mathbb{L}}\mathbf{z}$ denotes the orthogonal projection onto the tangent space.

3.2. Constructing Centripetal Hyperbolic Space

To address disordered cross-modality flows, we first align the latent geometry into a *centripetal hierarchy* (Figure 2a). Formally, let \mathbf{x}_1 denote the hyperbolic textual prototypes (serving as semantic roots/targets) and \mathbf{x}_0 denote the hyperbolic visual features (serving as entailment leaves/sources). This alignment resolves path entanglement by transforming arbitrary transport paths into ordered centripetal flows from \mathbf{x}_0 to \mathbf{x}_1 . The exponential boundary expansion guarantees sufficient initialization spacing for visual feature \mathbf{x}_0 , reducing spatial trajectory overlap during inward transport.

Geometric Stratification. We explicitly impose a centripetal hierarchy by initializing learnable scalars as: $\alpha_{\text{txt}} < \alpha_{\text{img}}$ to modulate the feature norm before tangent to manifold projection. This configuration anchors text near the origin and pushes images to the boundary (§Figure 2a), creating an explicit geometric prior for inward transport.

Centripetal hyperbolic alignment. To solidify this hierarchy, we optimize the embeddings using joint objectives that enforce both geometric entailment and semantic discrimination. In Figure 2a, we employ the *hyperbolic entailment loss* (Desai et al., 2023) to enforce a partial order where the text prototype \mathbf{x}_1 (parent) spatially entails the image feature \mathbf{x}_0 (child). Formally, we constrain \mathbf{x}_0 to lie within the entailment cone of \mathbf{x}_1 by minimizing the angular violation:

$$\mathcal{L}_{\text{entail}} = \max(0, \pi - \angle \mathbf{0}\mathbf{x}_1\mathbf{x}_0 - \omega(\mathbf{x}_1)), \quad (3)$$

where the term $\pi - \angle \mathbf{0}\mathbf{x}_1\mathbf{x}_0$ corresponds to the exterior angle at \mathbf{x}_1 , explicitly quantifying the deviation of the child \mathbf{x}_0 from the parent’s radial axis. The term $\omega(\mathbf{x}_1) = \arcsin(2H/\|\mathbf{x}_1\|_{\mathbb{L}})$ represents the cone aperture, which naturally narrows as the prototype’s radius increases.

Complementing this, we use a hyperbolic contrastive loss \mathcal{L}_{con} to enforce semantic discrimination. It minimizes the

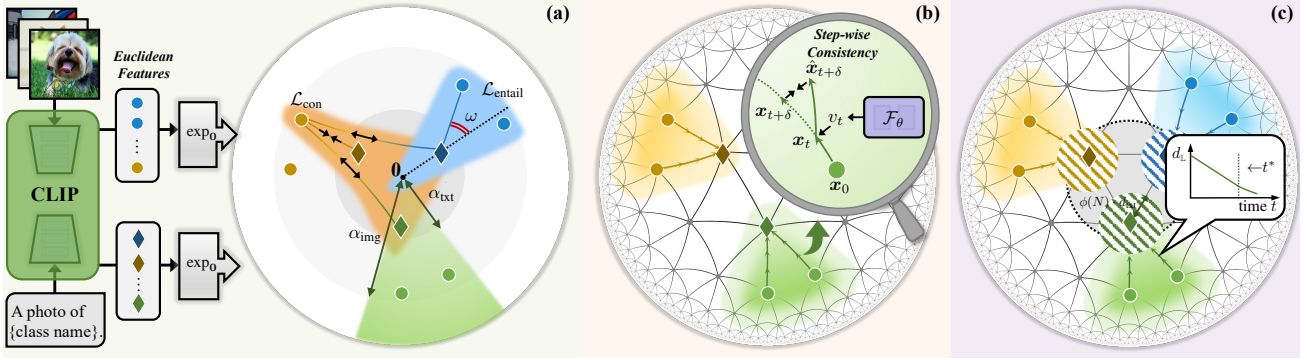


Figure 2. The overview of HFM. (a) **Constructing Centripetal Hyperbolic Space**: Establish a centripetal cross-modal hierarchy, optimizing textual roots near the origin and visual leaves toward the boundary. (b) **Learning Path-Decoupled Flows**: Tangent velocity fields \mathcal{F}_θ are optimized to guide features along isolated geodesic corridors. The step-wise consistency enforces trajectory decoupling in hyperbolic space. (c) **Inference with Diameter-based Stopping**: The flow terminates at t^* once the distance to text prototypes drops below a dynamic threshold scaled by semantic diameter d_{txt} to alleviate over-transportation into the crowded origin.

geodesic distance between the image feature \mathbf{x}_0 and its ground-truth text prototype \mathbf{x}_1^c , while maximizing distances to other prototypes in the support set:

$$\mathcal{L}_{\text{con}} = -\log \frac{\exp(-d_{\mathbb{L}}(\mathbf{x}_0, \mathbf{x}_1^c)/\tau)}{\sum_k \exp(-d_{\mathbb{L}}(\mathbf{x}_0, \mathbf{x}_1^k)/\tau)}. \quad (4)$$

3.3. Learning Path-Decoupled Flows

Having aligned the centripetal hierarchy, we proceed to learn the transport dynamics that guide entailment from visual leaves to semantic roots. Unlike standard Riemannian flow matching (Chen & Lipman, 2022) that typically requires integrating an ordinary differential equation (ODE) over a continuous velocity field, we propose path-decoupled HFM. Our core insight is to exploit *step-wise transport* (Yang et al., 2024) to enable explicit geometric supervision (§Figure 2b).

Geodesic Path. Similar to the plain Euclidean flow matching (Jiang et al., 2025), we define the ground-truth trajectory as the geodesic path on \mathbb{L} connecting the source image \mathbf{x}_0 explicitly to its ground-truth class prototype \mathbf{x}_1 . This strict pairing disentangles the optimization into independent source-target tasks, effectively eliminating inter-class interference (Jiang et al., 2025).

Tangent Velocity Alignment. To learn the transport dynamics, we sample paired states $(\mathbf{x}_t, \mathbf{x}_{t+\delta})$ from the ground-truth geodesic path. Specifically, given a random time t and a step size δ , we aim to predict the update that transports the feature from \mathbf{x}_t to $\mathbf{x}_{t+\delta}$. Our network \mathcal{F}_θ predicts an ambient vector at state \mathbf{x}_t , which is explicitly projected onto the local tangent space to ensure geometric validity:

$$\mathbf{v}_t = \Pi_{T_{\mathbf{x}_t}\mathbb{L}}(\mathcal{F}_\theta(\mathbf{x}_t, t)), \quad (5)$$

where $\Pi_{T_{\mathbf{x}_t}\mathbb{L}}$ denotes the orthogonal projection onto the tangent space at \mathbf{x}_t . We then model the discrete evolution by mapping this tangent velocity back onto the manifold via

the exponential map (Chen & Lipman, 2022):

$$\hat{\mathbf{x}}_{t+\delta} = \exp_{\mathbf{x}_t}^{\mathbb{L}}(\delta \cdot \mathbf{v}_t). \quad (6)$$

This parameterization ensures that the predicted next state $\hat{\mathbf{x}}_{t+\delta}$ strictly resides on the hyperbolic manifold \mathbb{L} .

Path-decoupled Objective. We optimize the network using a path-decoupled objective that enforces both step-wise trajectory consistency and semantic separation. Crucially, both losses operate on the predicted future state $\hat{\mathbf{x}}_{t+\delta}$, enabling direct rectification of the flow.

1) *Step-wise Consistency Loss*: To ensure the learned flow precisely follows the geodesic path, we minimize the squared Riemannian distance between the predicted state $\hat{\mathbf{x}}_{t+\delta}$ and the ground-truth target $\mathbf{x}_{t+\delta}$:

$$\mathcal{L}_{\text{step}} = \|d_{\mathbb{L}}(\hat{\mathbf{x}}_{t+\delta}, \mathbf{x}_{t+\delta})\|^2. \quad (7)$$

2) *Inter-Class Decoupling Loss*: To prevent the flow from drifting into the attraction basins of incorrect classes, we impose a “semantic guardrail” via a dynamic hyperbolic contrastive loss. Unlike the static alignment, this objective forces the predicted intermediate state $\hat{\mathbf{x}}_{t+\delta}$ to maximize its similarity with the corresponding prototype \mathbf{x}_1^c while repelling all negative prototypes:

$$\mathcal{L}_{\text{icd}} = -\log \frac{\exp(-d_{\mathbb{L}}(\hat{\mathbf{x}}_{t+\delta}, \mathbf{x}_1^c)/\tau)}{\sum_k \exp(-d_{\mathbb{L}}(\hat{\mathbf{x}}_{t+\delta}, \mathbf{x}_1^k)/\tau)}. \quad (8)$$

The total objective is $\mathcal{L} = \mathcal{L}_{\text{step}} + \lambda \mathcal{L}_{\text{icd}}$. The overall training procedure is summarized in Algorithm 1. By penalizing semantic deviations at each intermediate step, this mechanism strictly confines trajectories to class-specific corridors, thereby eliminating the path entanglement issue.

3.4. Inference with Diameter-based Stopping

During inference, we transport the visual features of test images along the predicted geodesic flow. To prevent over-

Algorithm 1 Training Path-Decoupled Flows

- 1: **Input:** paired hyperbolic image features and text features $\mathcal{D} = \{(\mathbf{x}_0, \mathbf{x}_1)\}$, stepsize δ , weight λ .
 - 2: **Initialize:** flow network parameters θ .
 - 3: **repeat**
 - 4: $t \sim \mathcal{U}([0, 1]), (\mathbf{x}_0, \mathbf{x}_1) \sim \mathcal{D}$
 - 5: $\mathbf{x}_t \leftarrow \exp_{\mathbf{x}_0}^{\kappa}(t \cdot \log_{\mathbf{x}_0}^{\kappa}(\mathbf{x}_1))$
 - 6: $\mathbf{x}_{t+\delta} \leftarrow \exp_{\mathbf{x}_0}^{\kappa}((t + \delta) \cdot \log_{\mathbf{x}_0}^{\kappa}(\mathbf{x}_1))$
 - 7: $\mathbf{v}_t \leftarrow \Pi_{T_{\hat{\mathbf{x}}_t} \mathbb{L}}(\mathcal{F}_{\theta}(\mathbf{x}_t, t))$
 - 8: $\hat{\mathbf{x}}_{t+\delta} \leftarrow \exp_{\hat{\mathbf{x}}_t}^{\kappa}(\delta \cdot \mathbf{v}_t)$
 - 9: $\mathcal{L} = \|d_{\mathbb{L}}(\hat{\mathbf{x}}_{t+\delta}, \mathbf{x}_{t+\delta})\|^2 + \lambda \mathcal{L}_{\text{icd}}$
 - 10: Update θ using gradient descent to minimize \mathcal{L}
 - 11: **until** converged
-

Algorithm 2 Inference with Diameter-based Stopping

- 1: **Input:** image feature \mathbf{x}_0 , text prototypes $\{\mathbf{x}_1^c\}$, trained flow network \mathcal{F}_{θ} , stepsize δ , class number N .
 - 2: **Initialize:** $t \leftarrow 0, d_{\text{txt}} = \max_{i,j} d_{\mathbb{L}}(\mathbf{x}_1^i, \mathbf{x}_1^j)$.
 - 3: **while** $t < 1$ **do**
 - 4: $\mathbf{v}_t \leftarrow \Pi_{T_{\hat{\mathbf{x}}_t} \mathbb{L}}(\mathcal{F}_{\theta}(\hat{\mathbf{x}}_t, t))$
 - 5: $\hat{\mathbf{x}}_{t+\delta} \leftarrow \exp_{\hat{\mathbf{x}}_t}^{\kappa}(\delta \cdot \mathbf{v}_t)$
 - 6: **if** $\min_c d_{\mathbb{L}}(\hat{\mathbf{x}}_{t+\delta}, \mathbf{x}_1^c) \leq \phi(N) \cdot d_{\text{txt}}$ **then**
 - 7: $t^* \leftarrow t + \delta$; **break**
 - 8: **end if**
 - 9: $t \leftarrow t + \delta$
 - 10: **end while**
 - 11: **return** $\hat{y} = \arg \min_c \sum_{t=0}^{t^*} d_{\mathbb{L}}(\hat{\mathbf{x}}_t, \mathbf{x}_1^c)$
-

shooting at the crowded hyperbolic boundary, we further propose an adaptive strategy comprising two steps:

Riemannian Euler Integration. We solve the transport ODE using a discrete Euler method (Lipman et al., 2022). Specifically, starting from the hyperbolic visual feature $\hat{\mathbf{x}}_0$, we iteratively update the state by projecting the predicted tangent velocity back onto the manifold:

$$\hat{\mathbf{x}}_{t+\delta} = \exp_{\hat{\mathbf{x}}_t}^{\kappa}(\delta \cdot \Pi_{T_{\hat{\mathbf{x}}_t} \mathbb{L}}(\mathcal{F}_{\theta}(\hat{\mathbf{x}}_t, t))). \quad (9)$$

Diameter-based Stopping. We define the semantic diameter d_{txt} as the maximum pairwise geodesic distance among all target prototypes $\{\mathbf{x}_1^c\}$. During inference, transport terminates at step t^* once the geodesic distance to the nearest prototype falls within a density-adaptive threshold:

$$\min_c d_{\mathbb{L}}(\hat{\mathbf{x}}_{t^*}, \mathbf{x}_1^c) \leq \phi(N) \cdot d_{\text{txt}}. \quad (10)$$

Here, $d_{\text{txt}} = \max_{i,j} d_{\mathbb{L}}(\mathbf{x}_1^i, \mathbf{x}_1^j)$ represents the intrinsic semantic scale, while $\phi(N) = 0.5 \log_{10}(N)$ compensates for manifold crowding as the class cardinality N grows.

To mitigate local fluctuations, instead of relying solely on the final state, we ensemble the class probabilities across all

valid steps up to t^* to determine the final prediction. The entire inference process is presented in Algorithm 2.

4. Experiments

Datasets. We evaluated HFM on standard few-shot image classification. Particularly, we conducted experiments on 11 benchmarks, including Aircraft (Maji et al., 2013), EuroSAT (Helber et al., 2019), DTD (Cimpoi et al., 2014), SUN397 (Xiao et al., 2010), UCF101 (Soomro et al., 2012), StanfordCars (Krause et al., 2013), ImageNet (Deng et al., 2009), Flowers102 (Nilsback & Zisserman, 2008), Food101 (Bossard et al., 2014), OxfordPets (Parkhi et al., 2012), and Caltech101 (Fei-Fei et al., 2004). Following prior works (Jiang et al., 2025), we partitioned them into two subsets: the first five datasets form the *difficult* group, while the remaining six constitute the *easy* group. For each dataset, we adopted the standard train/validation/test splits. Under the K -shot setting, we constructed the training set by uniformly sampling K labeled images per class, with the rest used for validation and testing according to the protocol.

Implementation Details. We implemented HFM on top of CLIP-LoRA (Zanella & Ben Ayed, 2024). Specifically, we first utilized the trained CLIP-LoRA model after centripetal hyperbolic alignment to extract image and text features, then trained a velocity network on these features following the HFM framework. Similar to FMA (Jiang et al., 2025), we adopted the lightweight architecture from MAR (Li et al., 2024) as our flow-matching network, implemented as a deep residual MLP with timestep conditioning. As for Lorentz model, we initialized the manifold curvature $\kappa = 1.0$ and $\alpha_{\text{txt}} = 0.5 \cdot \alpha_{\text{img}}$. Following (Desai et al., 2023), we set a constant $H=0.1$. The balance weight λ for the inter-class decoupling loss was set to 0.1. We optimized HFM with AdamW (Loshchilov & Hutter, 2017) using a learning rate of 2×10^{-4} and a cosine annealing schedule.

4.1. Quantitative Comparison

Settings. We compared HFM with recent few-shot classification methods including CLIP (Radford et al., 2021), CoOp (Zhou et al., 2022b), CoCoOp (Zhou et al., 2022a), TIP-Adapter (Zhang et al., 2022), CLIP-Adapter (Gao et al., 2024), PLOT++ (Chen et al., 2022a), KgCoOp (Yao et al., 2023), ProGrad (Zhu et al., 2023), CLIP-LoRA (Zanella & Ben Ayed, 2024) and FMA (Jiang et al., 2025). All methods use CLIP ViT-B/16 (Radford et al., 2021) as the backbone.

Results. As seen from Table 1, HFM consistently outperforms SOTA baselines across all settings. Crucially, HFM surpasses the Euclidean counterpart FMA (Jiang et al., 2025), verifying the efficacy of hyperbolic geometry in resolving path entanglement. On the difficult benchmarks, HFM achieves **64.1%** (1-shot) and **79.8%** (16-shot), ex-

Table 1. **Quantitative results.** Performance comparison (§4.1) of the state-of-the-art approaches. Based on CLIP-LoRA, we add HFM to further improve the performance. Top-1 accuracy averaged over 3 random seeds is reported. The highest value of each dataset is bolded.

Shots	Method	Difficult						Easy						
		Aircraft	SAT	DTD	SUN	UCF	Avg	Cars	Net	Flowers	Food	Pets	Caltech	Avg
0	CLIP 2021	24.8	47.8	43.8	62.5	66.7	47.6	65.5	66.7	67.4	85.3	89.1	92.9	77.7
	CoOp 2022b	20.8	56.4	50.1	67.0	71.2	53.1	67.5	65.7	78.3	84.3	90.2	92.5	79.8
	CoCoOp 2022a	28.1	55.4	52.6	68.7	70.4	55.0	67.6	69.4	73.4	84.9	91.9	94.1	80.2
	TIP-Adapter 2022	28.8	67.8	51.6	67.2	73.4	57.8	67.1	69.4	83.8	85.8	90.6	94.0	81.8
	CLIP-Adapter 2024	25.2	49.3	44.2	65.4	66.9	50.2	65.7	67.9	71.3	86.1	89.0	92.0	78.7
	PLOT++ 2022a	28.6	65.4	54.6	66.8	74.3	58.0	68.8	66.5	80.5	86.2	91.9	94.3	81.4
	KgCoOp 2023	26.8	61.9	52.7	68.4	72.8	56.5	66.7	68.9	74.7	86.4	92.1	94.2	80.5
	ProGrad 2023	28.9	57.0	52.8	67.0	73.3	55.8	68.2	67.0	80.9	84.9	91.4	93.5	81.0
	CLIP-LoRA 2024	28.0	71.9	54.1	70.3	75.4	59.9	69.4	70.3	81.4	85.1	91.9	93.8	82.0
	+FMA 2025	28.3	73.0	55.1	70.6	75.9	60.6 ^{+0.7}	69.8	70.2	84.9	85.2	92.1	94.5	82.8 ^{+0.8}
+HFM (Ours)	32.2	81.0	58.6	71.4	77.4	64.1^{+4.2}	70.3	70.0	86.2	85.4	92.0	95.2	83.2^{+1.2}	
1	CoOp 2022b	30.9	69.7	59.5	69.7	77.6	61.5	74.4	68.8	92.2	84.5	92.5	94.5	84.5
	CoCoOp 2022a	30.6	61.7	55.7	70.4	75.3	58.7	69.5	70.6	81.5	86.3	92.7	94.8	82.6
	TIP-Adapter 2022	35.7	76.8	59.8	70.8	78.1	64.2	74.1	70.7	92.1	86.5	91.9	94.8	85.0
	CLIP-Adapter 2024	27.9	51.2	46.1	68.0	70.6	52.8	67.5	68.6	73.1	86.5	90.8	94.0	80.1
	PLOT++ 2022a	35.3	83.2	62.4	71.7	79.8	66.5	76.3	70.4	92.9	86.5	92.7	95.1	85.6
	KgCoOp 2023	32.2	71.8	58.7	71.5	77.6	62.4	69.5	69.9	87.0	86.9	92.6	95.0	83.5
	ProGrad 2024	34.1	69.6	59.7	71.7	77.9	62.6	75.0	70.2	91.1	85.4	92.1	94.4	84.7
	CLIP-LoRA 2024	38.8	83.5	64.0	72.8	81.1	68.0	77.4	71.4	92.9	82.6	90.6	95.0	85.0
	+FMA 2025	40.3	85.0	67.0	73.7	82.4	69.7 ^{+1.7}	78.9	72.0	95.0	83.2	90.8	95.8	86.0 ^{+1.0}
	+HFM (Ours)	43.5	90.3	68.6	75.5	83.6	72.3^{+4.3}	80.1	72.1	96.2	86.9	93.2	96.2	87.4^{+2.4}
4	CoOp 2022b	43.3	86.0	70.0	74.9	83.1	71.4	83.1	71.4	97.2	84.4	91.1	95.5	87.1
	CoCoOp 2022a	33.8	75.5	65.8	72.8	76.0	64.8	72.4	71.1	87.1	87.4	93.2	95.2	84.4
	TIP-Adapter 2022	44.6	85.9	70.8	76.0	83.9	72.2	82.3	73.4	96.2	86.8	92.6	95.7	87.8
	CLIP-Adapter 2024	34.2	71.4	59.4	74.2	80.2	63.9	74.0	69.8	92.9	87.1	92.3	94.9	85.2
	PLOT++ 2022a	46.7	92.0	71.4	76.0	85.3	74.3	84.6	72.6	97.6	87.1	93.6	96.0	88.6
	KgCoOp 2023	36.5	76.2	68.7	73.3	81.7	67.3	74.8	70.4	93.4	87.2	93.2	95.2	85.7
	ProGrad 2024	43.0	83.6	68.8	75.1	82.7	70.6	82.9	72.1	96.6	85.8	92.8	95.9	87.7
	CLIP-LoRA 2024	54.7	90.7	73.0	76.0	86.2	76.1	86.0	73.4	97.9	84.2	91.6	96.1	88.2
	+FMA 2025	57.8	91.0	75.4	77.2	87.1	77.7 ^{+1.6}	87.7	73.5	99.1	85.1	91.6	96.5	88.9 ^{+0.7}
	+HFM (ours)	62.1	94.3	76.0	77.5	88.9	79.8^{+3.7}	88.6	73.6	98.7	87.2	94.1	96.8	89.8^{+1.6}
16	CoOp 2022b	43.3	86.0	70.0	74.9	83.1	71.4	83.1	71.4	97.2	84.4	91.1	95.5	87.1
	CoCoOp 2022a	33.8	75.5	65.8	72.8	76.0	64.8	72.4	71.1	87.1	87.4	93.2	95.2	84.4
	TIP-Adapter 2022	44.6	85.9	70.8	76.0	83.9	72.2	82.3	73.4	96.2	86.8	92.6	95.7	87.8
	CLIP-Adapter 2024	34.2	71.4	59.4	74.2	80.2	63.9	74.0	69.8	92.9	87.1	92.3	94.9	85.2
	PLOT++ 2022a	46.7	92.0	71.4	76.0	85.3	74.3	84.6	72.6	97.6	87.1	93.6	96.0	88.6
	KgCoOp 2023	36.5	76.2	68.7	73.3	81.7	67.3	74.8	70.4	93.4	87.2	93.2	95.2	85.7
	ProGrad 2024	43.0	83.6	68.8	75.1	82.7	70.6	82.9	72.1	96.6	85.8	92.8	95.9	87.7
	CLIP-LoRA 2024	54.7	90.7	73.0	76.0	86.2	76.1	86.0	73.4	97.9	84.2	91.6	96.1	88.2
	+FMA 2025	57.8	91.0	75.4	77.2	87.1	77.7 ^{+1.6}	87.7	73.5	99.1	85.1	91.6	96.5	88.9 ^{+0.7}
	+HFM (ours)	62.1	94.3	76.0	77.5	88.9	79.8^{+3.7}	88.6	73.6	98.7	87.2	94.1	96.8	89.8^{+1.6}

ceeding FMA by **3.5%** and **2.1%**, respectively. This advantage is most pronounced on structurally complex datasets like EuroSAT and DTD, where HFM outperforms FMA by **8.0%** and **3.5%** under the 1-shot setting. Furthermore, compared to the strong CLIP-LoRA (Zanella & Ben Ayed, 2024) baseline, HFM yields consistent gains of **3.7%**–**4.3%** on difficult datasets, demonstrating the superiority of continuous flow adaptation over static parameter tuning.

4.2. Diagnostic Experiments

To verify the efficacy of HFM and each module, we performed extensive diagnostic experiments.

Key Component Analysis. Contributions of Centripetal Hyperbolic Alignment (CHA), flowing matching with Path-decoupled Objective (PO), and inference with Diameter-based Stopping (DS) were evaluated under both 4-shot and 16-shot settings, as summarized in Table 2. The first row in each block refers to the baseline model (*i.e.*, CLIP-LoRA (Zanella & Ben Ayed, 2024)) implemented in Eu-

clidean space. Taking the 16-shot setting as an example, four crucial conclusions can be drawn. **First**, by simply restructuring the latent space with CHA, consistent improvements are observed, with notable gains on the challenging Aircraft benchmark (from 54.7% to **56.9%**). This demonstrates that the concentric hierarchy, *i.e.*, anchoring text as roots and images as leaves, provides a superior geometric initialization than the unstructured Euclidean space. **Second**, with the guidance of the path-decoupled objective in flow matching, the model effectively learns to decouple transport trajectories, resulting in a substantial performance leap (*e.g.*, **61.4%** on Aircraft). This indicates that the “semantic guardrail” mechanism successfully reduces inter-class interference by confining features to isolated geodesic corridors. **Third**, benefiting from the adaptive diameter-based stopping, the inference process terminates dynamically based on the intrinsic semantic scale. This yields further improvements (*e.g.*, **62.1%** on Aircraft), confirming that preventing over-transportation into the crowded origin is essential for preserving discriminability. **Finally**, this progressive im-

Table 2. **Ablation Study.** Analysis of component effectiveness (§4.2) under 4/16-shot settings. **CHA**: Centripetal Hyperbolic Alignment to construct the centripetal hierarchy, **PO**: flow matching with the Path-decoupled Objective, **DS**: inference with Diameter-based Stopping.

Shots	Components			Difficult Datasets					Easy Datasets							
	CHA	PO	DS	FGVC	EuroSAT	DTD	SUN	UCF	Avg	Cars	Net	Flowers	Food	Pets	Caltech	Avg
4	x	x	x	38.8	83.5	64.0	72.8	81.1	68.0	77.4	71.4	92.9	82.6	90.6	95.0	85.0
	✓	x	x	38.9	88.4	65.9	74.0	81.8	69.8	77.6	71.4	94.4	86.7	92.6	95.7	86.4
	✓	✓	x	43.5	88.6	68.0	75.4	83.6	71.8	80.5	71.9	96.4	86.8	92.7	95.8	87.3
	✓	✓	✓	43.5	90.3	68.6	75.5	83.6	72.3	80.1	72.1	96.2	86.9	93.2	96.2	87.4
16	x	x	x	54.7	90.7	73.0	76.0	86.2	76.1	86.0	73.4	97.9	84.2	91.6	96.1	88.2
	✓	x	x	56.9	93.2	74.1	76.9	87.6	77.7	86.6	73.6	98.4	87.3	93.5	96.4	89.3
	✓	✓	x	61.4	93.2	76.4	77.5	87.3	79.2	88.5	74.3	98.5	87.4	93.7	96.5	89.8
	✓	✓	✓	62.1	94.3	76.0	77.5	88.9	79.8	88.6	73.6	98.7	87.2	94.1	96.8	89.8

Table 3. **Ablation Study.** Analysis of model-agnostic capability (§4.2) across various PEFT approaches under the 16-shot setting.

Method	Difficult						Easy						
	Aircraft	SAT	DTD	SUN	UCF	Avg	Cars	Net	Flowers	Food	Pets	Caltech	Avg
CoOp 2022b	43.3	86.0	70.0	74.9	83.1	71.4	83.1	71.4	97.2	84.4	91.1	95.5	87.1
+FMA 2025	47.6	88.1	73.1	75.9	84.4	73.8+2.4	85.4	72.5	98.2	85.0	91.4	95.7	88.0+0.9
+HFM (ours)	49.2	88.9	75.1	76.4	84.7	74.9+3.5	84.9	72.2	98.2	86.6	93.8	96.3	88.7+1.6
CoCoOp 2022a	33.8	75.5	65.8	72.8	76.0	64.8	72.4	71.1	87.1	87.4	93.2	95.2	84.4
+FMA 2025	36.9	86.9	71.9	73.4	80.3	69.9+5.1	73.5	71.9	94.5	87.8	93.4	95.6	86.1+1.7
+HFM (ours)	43.7	89.3	72.6	75.6	83.9	73.0+8.2	79.3	71.9	97.9	87.1	93.9	96.3	87.7+3.3
CLIP-Adapter 2024	33.8	70.4	59.3	74.3	80.1	63.6	74.2	71.6	93.6	87.1	92.4	94.9	85.6
+FMA 2025	35.8	85.6	69.2	74.4	81.5	69.3+5.7	74.7	71.3	95.6	87.2	92.9	96.0	86.3+0.7
+HFM (ours)	43.8	85.7	71.4	76.1	84.6	72.3+8.7	80.6	72.1	97.2	87.0	93.3	96.2	87.7+2.1
CLIP-LoRA 2024	54.7	90.7	73.0	76.0	86.2	76.1	86.0	73.4	97.9	84.2	91.6	96.1	88.2
+FMA 2025	57.8	91.0	75.4	77.2	87.1	77.7+1.6	87.7	73.5	99.1	85.1	91.6	96.5	88.9+0.7
+HFM (ours)	62.1	94.3	76.0	77.5	88.9	79.8+3.7	88.6	73.6	98.7	87.2	94.1	96.8	89.8+1.6

provement is consistent across different data settings. For the difficult datasets, the average accuracy increases from 68.0% to **72.3%** in 4-shot setting, paralleling the trend in the 16-shot setting (76.1% to **79.8%**). This consistency verifies that HFM is robust to data scarcity and can effectively resolve path-entanglement regardless of the support set size.

Model-Agnostic Generalization. We investigated the generalizability of HFM by integrating it with various PEFT architectures, as shown in Table 3. As a plug-and-play module, HFM consistently yields superior performance when applied to CoOp (Zhou et al., 2022b), CoCoOp (Zhou et al., 2022a), CLIP-Adapter (Gao et al., 2024), and CLIP-LoRA (Zanella & Ben Ayed, 2024). For instance, when equipping CLIP-Adapter (Gao et al., 2024) with HFM, the average accuracy on difficult datasets yields a remarkable surge of **8.7%** (from 63.6% to 72.3%), significantly outperforming the **5.7%** gain obtained by the Euclidean counterpart FMA (Jiang et al., 2025). Similarly, on CoCoOp (Zhou et al., 2022a), HFM achieves an **8.2%** improvement, surpassing FMA by a clear margin of **3.1%**. Even on the stronger CoOp (Zhou et al., 2022b) baseline, HFM provides a consistent **3.5%** gain on difficult benchmarks. These results confirm that the benefit of hyperbolic geometry is orthogonal to the choice of parameter-tuning strategy, serving as a universal geometric enhancer for resolving path-entanglement.

Scalability across Backbones. Table 4 reports the performance using different CLIP backbones (ViT-B/32, ViT-B/16, and ViT-L/14) under both 4/16-shot settings. HFM consistently enhances the baseline CLIP-LoRA across all model sizes. Specifically, on the difficult benchmarks, HFM achieves remarkable accuracy gains. For instance, with the ViT-B/32 backbone, our method improves performance by **2.6%** (72.3% vs. 74.9%) in the 16-shot setting. This advantage scales effectively to the larger ViT-L/14 model, where HFM yields consistent improvements of **2.1%** (81.0% vs. 83.1%) on difficult datasets, while reaching a peak average accuracy of **93.1%** on the easy group. Furthermore, in the data-scarce 4-shot setup, HFM boosts the widely used ViT-B/16 backbone by a substantial margin of **4.3%** on difficult groups. This demonstrates that our method scales effectively with model capacity and feature dimensionality, maintaining its superiority even with stronger visual encoders.

4.3. Qualitative Comparison

To intuitively understand how HFM resolves path entanglement, we visualized the transport trajectories on five difficult benchmarks using PCA. As illustrated in Figure 3, we can observe that: 1) **Chaotic Crossovers in Euclidean Flows.** The top row reveals that Euclidean flow matching suffers from severe *path entanglement*. Due to the limited spatial

Table 4. **Ablation study.** Performance comparison (§4.2) between CLIP-LoRA and our HFM on different backbones (ViT-B32, ViT-B16, and ViT-L14) with 4 and 16 shots. Top-1 accuracy is reported. The highest value of each setting is bolded.

Shots	Backbone	Method	Difficult						Easy						
			Aircraft	SAT	DTD	SUN	UCF	Avg	Cars	Net	Flowers	Food	Pets	Caltech	Avg
4	ViT-B32	CLIP-LoRA 2024	27.7	85.6	60.3	70.3	76.5	64.1	68.3	66.5	90.1	75.6	86.3	94.3	80.2
		+HFM (ours)	33.9	90.1	64.5	72.7	80.1	68.3+4.2	71.6	66.7	93.1	80.7	90.6	95.4	83.0+2.8
	ViT-B16	CLIP-LoRA 2024	38.8	83.5	64.0	72.8	81.1	68.0	77.4	71.4	92.9	82.6	90.6	95.0	85.0
		+HFM (ours)	43.5	90.3	68.6	75.5	83.6	72.3+4.3	80.1	72.1	96.2	86.9	93.2	96.2	87.4+2.4
	ViT-L14	CLIP-LoRA 2024	48.9	86.4	70.4	76.7	86.4	73.8	85.2	77.9	97.4	89.6	93.9	97.2	90.2
		+HFM (ours)	54.8	88.6	72.2	78.9	88.3	76.6+2.8	87.0	78.9	98.7	91.8	95.3	97.7	91.6+1.4
16	ViT-B32	CLIP-LoRA 2024	44.9	91.8	68.2	74.0	82.8	72.3	79.7	68.4	96.2	78.2	88.8	95.2	84.4
		+HFM (ours)	50.4	93.1	71.0	75.0	85.2	74.9+2.6	81.8	68.5	97.3	81.0	89.3	95.9	85.6+1.2
	ViT-B16	CLIP-LoRA 2024	54.7	90.7	73.0	76.0	86.2	76.1	86.0	73.4	97.9	84.2	91.6	96.1	88.2
		+HFM (ours)	62.1	94.3	76.0	77.5	88.9	79.8+3.7	88.6	73.6	98.7	87.3	94.1	96.8	89.8+1.6
	ViT-L14	CLIP-LoRA 2024	66.2	93.1	76.5	79.4	89.9	81.0	90.9	79.6	99.0	89.9	94.3	97.3	91.8
		+HFM (ours)	68.7	93.4	80.1	81.6	91.5	83.1+2.1	92.0	80.7	99.3	92.2	96.2	98.0	93.1+1.3

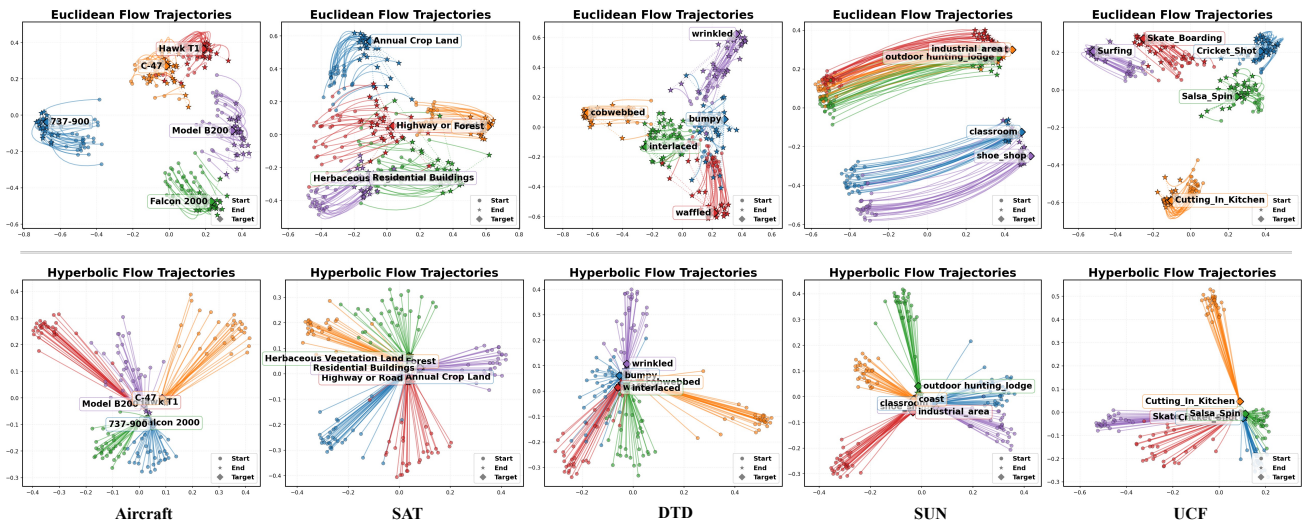


Figure 3. **Qualitative Results.** Visualization of transport trajectories (§4.3). **Top:** Euclidean flows suffer from severe *path entanglement*, exhibiting chaotic and intersecting paths due to spatial crowding. **Bottom:** HFM achieves *path decoupling* via a *centripetal hierarchy*. Visual features move centripetally from the boundary to central text roots along isolated geodesic corridors.

capacity of flat geometry, trajectories from different classes are densely packed and frequently intersect. For instance, in the Aircraft and DTD datasets, the flow paths of neighboring categories (*e.g.*, different textures or aircraft models) exhibit chaotic crossovers, leading to ambiguous decision boundaries and potential misclassification. 2) **Ordered Decoupling in Hyperbolic Flows.** In contrast, the bottom row demonstrates that HFM generates highly organized, radial trajectories. Driven by our *centripetal hyperbolic alignment*, the visual features are transported from the boundary inward to the central text roots along isolated geodesic corridors. This structure effectively exploits the exponential volume expansion of the Lorentz manifold to separate diverse semantic clusters. Consequently, inter-class collisions are virtually eliminated, confirming the efficacy of our path-decoupled objective in preserving semantic discriminability during the adaptation process.

5. Conclusion

In this paper, we identified that the polynomial volume growth of Euclidean space limits existing flow matching methods, leading to severe path entanglement in few-shot adaptation. To this end, we proposed path-decoupled Hyperbolic Flow Matching (HFM), which exploits the exponential expansion of the Lorentz manifold to decouple transport trajectories. Through centripetal hyperbolic alignment, a path-decoupled objective, and adaptive diameter-based stopping, HFM constructs isolated geodesic corridors and ensures precise inference termination. Empirical results on 11 benchmarks confirm that HFM not only establishes a new state-of-the-art but also demonstrates remarkable data efficiency in complex visual scenarios. We hope this work encourages further exploration into non-Euclidean generative dynamics for robust cross-modal understanding.

Impact Statements

This paper presents work whose goal is to advance the field of machine learning. There are many potential societal consequences of our work, none of which we feel must be specifically highlighted here.

References

- Alayrac, J.-B., Donahue, J., Luc, P., Miech, A., Barr, I., Hasson, Y., Lenc, K., Mensch, A., Millican, K., Reynolds, M., et al. Flamingo: a visual language model for few-shot learning. *Advances in neural information processing systems*, 35:23716–23736, 2022.
- Albergo, M. S., Boffi, N. M., and Vanden-Eijnden, E. Stochastic interpolants: A unifying framework for flows and diffusions. *arXiv preprint arXiv:2303.08797*, 2023.
- Atigh, M. G., Schoep, J., Acar, E., Van Noord, N., and Mettes, P. Hyperbolic image segmentation. In *Proceedings of the IEEE/CVF conference on computer vision and pattern recognition*, pp. 4453–4462, 2022.
- Bossard, L., Guillaumin, M., and Van Gool, L. Food-101—mining discriminative components with random forests. In *European conference on computer vision*, pp. 446–461. Springer, 2014.
- Cai, C., Wang, Q., Liang, B., Qin, B., Yang, M., Wong, K.-F., and Xu, R. In-context learning for few-shot multimodal named entity recognition. In *Findings of the Association for Computational Linguistics: EMNLP 2023*, pp. 2969–2979, 2023.
- Chen, G., Yao, W., Song, X., Li, X., Rao, Y., and Zhang, K. Plot: Prompt learning with optimal transport for vision-language models. *arXiv preprint arXiv:2210.01253*, 2022a.
- Chen, R. T. and Lipman, Y. Flow matching on general geometries. In *ICLR*, 2022.
- Chen, W., Han, X., Lin, Y., Zhao, H., Liu, Z., Li, P., Sun, M., and Zhou, J. Fully hyperbolic neural networks. In *Proceedings of the 60th Annual Meeting of the Association for Computational Linguistics (Volume 1: Long Papers)*, pp. 5672–5686, 2022b.
- Chen, W.-Y., Liu, Y.-C., Kira, Z., Wang, Y.-C. F., and Huang, J.-B. A closer look at few-shot classification, 2020. URL <https://arxiv.org/abs/1904.04232>.
- Cimpoi, M., Maji, S., Kokkinos, I., Mohamed, S., and Vedaldi, A. Describing textures in the wild. In *Proceedings of the IEEE conference on computer vision and pattern recognition*, pp. 3606–3613, 2014.
- De Marinis, P., Vessio, G., and Castellano, G. Take a peek: Efficient encoder adaptation for few-shot semantic segmentation via lora. *arXiv preprint arXiv:2512.10521*, 2025.
- Deng, J., Dong, W., Socher, R., Li, L.-J., Li, K., and Fei-Fei, L. Imagenet: A large-scale hierarchical image database. In *2009 IEEE conference on computer vision and pattern recognition*, pp. 248–255. Ieee, 2009.
- Desai, K., Nickel, M., Rajpurohit, T., Johnson, J., and Vedantam, S. R. Hyperbolic image-text representations. In *International Conference on Machine Learning*, pp. 7694–7731. PMLR, 2023.
- Dhingra, B., Shallue, C., Norouzi, M., Dai, A., and Dahl, G. Embedding text in hyperbolic spaces. In *Proceedings of the Twelfth Workshop on Graph-Based Methods for Natural Language Processing (TextGraphs-12)*, pp. 59–69, 2018.
- Esser, P., Kulal, S., Blattmann, A., Entezari, R., Müller, J., Saini, H., Levi, Y., Lorenz, D., Sauer, A., Boesel, F., et al. Scaling rectified flow transformers for high-resolution image synthesis. In *Forty-first international conference on machine learning*, 2024.
- Fei-Fei, L., Fergus, R., and Perona, P. Learning generative visual models from few training examples: An incremental bayesian approach tested on 101 object categories. In *2004 conference on computer vision and pattern recognition workshop*, pp. 178–178. IEEE, 2004.
- Gao, P., Geng, S., Zhang, R., Ma, T., Fang, R., Zhang, Y., Li, H., and Qiao, Y. Clip-adapter: Better vision-language models with feature adapters. *International Journal of Computer Vision*, 132(2):581–595, 2024.
- Gu, Y., Han, X., Liu, Z., and Huang, M. Ppt: Pre-trained prompt tuning for few-shot learning. In *Proceedings of the 60th annual meeting of the association for computational linguistics (volume 1: long papers)*, pp. 8410–8423, 2022.
- Helber, P., Bischke, B., Dengel, A., and Borth, D. Eurosat: A novel dataset and deep learning benchmark for land use and land cover classification. *IEEE Journal of Selected Topics in Applied Earth Observations and Remote Sensing*, 12(7):2217–2226, 2019.
- Ho, J., Jain, A., and Abbeel, P. Denoising diffusion probabilistic models. *Advances in neural information processing systems*, 33:6840–6851, 2020.
- Hong, J., Hayder, Z., Han, J., Fang, P., Harandi, M., and Petersson, L. Hyperbolic audio-visual zero-shot learning. In *Proceedings of the IEEE/CVF international conference on computer vision*, pp. 7873–7883, 2023.

- Hou, R., Chang, H., Ma, B., Shan, S., and Chen, X. Cross attention network for few-shot classification. *Advances in neural information processing systems*, 32, 2019.
- Hu, E. J., Shen, Y., Wallis, P., Allen-Zhu, Z., Li, Y., Wang, S., Wang, L., Chen, W., et al. Lora: Low-rank adaptation of large language models. *ICLR*, 1(2):3, 2022a.
- Hu, T., Meinel, C., and Yang, H. Scaled prompt-tuning for few-shot natural language generation. *arXiv preprint arXiv:2309.06759*, 2023.
- Hu, Y., Lee, C.-H., Xie, T., Yu, T., Smith, N. A., and Ostendorf, M. In-context learning for few-shot dialogue state tracking. *arXiv preprint arXiv:2203.08568*, 2022b.
- Huang, H., Xie, Y., Gao, J., Fan, C., and Cao, Z. Select and order: Optimizing few-shot image classification with in-context learning. In *International Conference on Multimedia Modeling*, pp. 425–438. Springer, 2024.
- Jia, C., Yang, Y., Xia, Y., Chen, Y.-T., Parekh, Z., Pham, H., Le, Q., Sung, Y.-H., Li, Z., and Duerig, T. Scaling up visual and vision-language representation learning with noisy text supervision. In *International conference on machine learning*, pp. 4904–4916. PMLR, 2021.
- Jiang, Z., Wang, Y., and Chen, L. Exploring cross-modal flows for few-shot learning. *arXiv preprint arXiv:2510.14543*, 2025.
- Khrulkov, V., Mirvakhabova, L., Ustinova, E., Oseledets, I., and Lempitsky, V. Hyperbolic image embeddings. In *Proceedings of the IEEE/CVF conference on computer vision and pattern recognition*, pp. 6418–6428, 2020.
- Krause, J., Stark, M., Deng, J., and Fei-Fei, L. 3d object representations for fine-grained categorization. In *Proceedings of the IEEE international conference on computer vision workshops*, pp. 554–561, 2013.
- Le, M., Roller, S., Papaxanthos, L., Kiela, D., and Nickel, M. Inferring concept hierarchies from text corpora via hyperbolic embeddings. In *Proceedings of the 57th annual meeting of the association for computational linguistics*, pp. 3231–3241, 2019.
- Lee, D., Song, S., Suh, J., Choi, J., Lee, S., and Kim, H. J. Read-only prompt optimization for vision-language few-shot learning. In *Proceedings of the IEEE/CVF international conference on computer vision*, pp. 1401–1411, 2023.
- Li, J., Wang, J., Tan, C., Lian, N., Chen, L., Wang, Y., Zhang, M., Xia, S.-T., and Chen, B. Enhancing partially relevant video retrieval with hyperbolic learning. In *Proceedings of the IEEE/CVF International Conference on Computer Vision*, pp. 23074–23084, 2025a.
- Li, J., Wang, J., Tan, C., Lian, N., Chen, L., Wang, Y., Zhang, M., Xia, S.-T., and Chen, B. Hlformer: Enhancing partially relevant video retrieval with hyperbolic learning. *arXiv preprint arXiv:2507.17402*, 2025b.
- Li, L., Zhang, Y., and Wang, S. The euclidean space is evil: Hyperbolic attribute editing for few-shot image generation. In *Proceedings of the IEEE/CVF international conference on computer vision*, pp. 22714–22724, 2023.
- Li, L., Li, J., Lei, J., Xiao, J., Shao, F., and Chen, L. H2em: Learning hierarchical hyperbolic embeddings for compositional zero-shot learning. *arXiv preprint arXiv:2512.20029*, 2025c.
- Li, L. H., Zhang, P., Zhang, H., Yang, J., Li, C., Zhong, Y., Wang, L., Yuan, L., Zhang, L., Hwang, J.-N., et al. Grounded language-image pre-training. In *CVPR*, pp. 10965–10975, 2022.
- Li, T., Tian, Y., Li, H., Deng, M., and He, K. Autoregressive image generation without vector quantization. In *NeurIPS*, 2024.
- Lipman, Y., Chen, R. T., Ben-Hamu, H., Nickel, M., and Le, M. Flow matching for generative modeling. *arXiv preprint arXiv:2210.02747*, 2022.
- Liu, Q., Nickel, M., and Kiela, D. Hyperbolic graph neural networks. *Advances in neural information processing systems*, 32, 2019.
- Liu, S., Chen, J., Pan, L., Ngo, C.-W., Chua, T.-S., and Jiang, Y.-G. Hyperbolic visual embedding learning for zero-shot recognition. In *Proceedings of the IEEE/CVF conference on computer vision and pattern recognition*, pp. 9273–9281, 2020.
- Liu, X., Gong, C., and Liu, Q. Flow straight and fast: Learning to generate and transfer data with rectified flow. *arXiv preprint arXiv:2209.03003*, 2022.
- Loshchilov, I. and Hutter, F. Decoupled weight decay regularization. *arXiv preprint arXiv:1711.05101*, 2017.
- Luo, Y., Du, D., Huang, H., Fang, Y., and Wang, M. Curveflow: Curvature-guided flow matching for image generation. *arXiv preprint arXiv:2508.15093*, 2025.
- Maji, S., Rahtu, E., Kannala, J., Blaschko, M., and Vedaldi, A. Fine-grained visual classification of aircraft. *arXiv preprint arXiv:1306.5151*, 2013.
- Nakashima, F., Nakamura, T., Takamune, N., Fukayama, S., and Saruwatari, H. Hyperbolic timbre embedding for musical instrument sound synthesis based on variational autoencoders. In *2022 Asia-Pacific Signal and Information Processing Association Annual Summit and Conference (APSIPA ASC)*, pp. 735–742. IEEE, 2022.

- Nickel, M. and Kiela, D. Poincaré embeddings for learning hierarchical representations. *Advances in neural information processing systems*, 30, 2017.
- Nickel, M. and Kiela, D. Learning continuous hierarchies in the lorentz model of hyperbolic geometry. In *International conference on machine learning*, pp. 3779–3788. PMLR, 2018.
- Nilsback, M.-E. and Zisserman, A. Automated flower classification over a large number of classes. In *2008 Sixth Indian conference on computer vision, graphics & image processing*, pp. 722–729. IEEE, 2008.
- Pal, A., van Spengler, M., di Melendugno, G. M. D., Flaborea, A., Galasso, F., and Mettes, P. Compositional entailment learning for hyperbolic vision-language models. In *ICLR*, 2025.
- Parkhi, O. M., Vedaldi, A., Zisserman, A., and Jawahar, C. Cats and dogs. In *2012 IEEE conference on computer vision and pattern recognition*, pp. 3498–3505. IEEE, 2012.
- Petermann, D., Wichern, G., Subramanian, A., and Le Roux, J. Hyperbolic audio source separation. In *ICASSP 2023-2023 IEEE International Conference on Acoustics, Speech and Signal Processing (ICASSP)*, pp. 1–5. IEEE, 2023.
- Radford, A., Kim, J. W., Hallacy, C., Ramesh, A., Goh, G., Agarwal, S., Sastry, G., Askell, A., Mishkin, P., Clark, J., et al. Learning transferable visual models from natural language supervision. In *International conference on machine learning*, pp. 8748–8763. PmLR, 2021.
- Ren, S., Yu, Q., He, J., Shen, X., Yuille, A., and Chen, L.-C. Flower: Scale-wise autoregressive image generation meets flow matching. *arXiv preprint arXiv:2412.15205*, 2024.
- Rombach, R., Blattmann, A., Lorenz, D., Esser, P., and Ommer, B. High-resolution image synthesis with latent diffusion models. In *Proceedings of the IEEE/CVF conference on computer vision and pattern recognition*, pp. 10684–10695, 2022.
- Song, Y., Sohl-Dickstein, J., Kingma, D. P., Kumar, A., Ermon, S., and Poole, B. Score-based generative modeling through stochastic differential equations. *arXiv preprint arXiv:2011.13456*, 2020.
- Soomro, K., Zamir, A. R., and Shah, M. Ucf101: A dataset of 101 human actions classes from videos in the wild. *arXiv preprint arXiv:1212.0402*, 2012.
- Wang, Y., Yao, Q., Kwok, J. T., and Ni, L. M. Generalizing from a few examples: A survey on few-shot learning. *ACM computing surveys (csur)*, 53(3):1–34, 2020.
- Wen, J., Chen, Y., Shi, R., Ji, W., Yang, M., Gao, D., Yuan, J., and Zimmermann, R. Hover: Hyperbolic video-text retrieval. *IEEE Transactions on Image Processing*, 2025.
- Xiao, J., Hays, J., Ehinger, K. A., Oliva, A., and Torralba, A. Sun database: Large-scale scene recognition from abbey to zoo. In *2010 IEEE computer society conference on computer vision and pattern recognition*, pp. 3485–3492. IEEE, 2010.
- Yang, L., Zhang, Z., Zhang, Z., Liu, X., Xu, M., Zhang, W., Meng, C., Ermon, S., and Cui, B. Consistency flow matching: Defining straight flows with velocity consistency. *arXiv preprint arXiv:2407.02398*, 2024.
- Yao, H., Zhang, R., and Xu, C. Visual-language prompt tuning with knowledge-guided context optimization. In *Proceedings of the IEEE/CVF conference on computer vision and pattern recognition*, pp. 6757–6767, 2023.
- Zanella, M. and Ben Ayed, I. Low-rank few-shot adaptation of vision-language models. In *Proceedings of the IEEE/CVF Conference on Computer Vision and Pattern Recognition*, pp. 1593–1603, 2024.
- Zhang, R., Zhang, W., Fang, R., Gao, P., Li, K., Dai, J., Qiao, Y., and Li, H. Tip-adapter: Training-free adaptation of clip for few-shot classification. In *European conference on computer vision*, pp. 493–510. Springer, 2022.
- Zhang, Z., Zhang, A., Li, M., Zhao, H., Karypis, G., and Smola, A. Multimodal chain-of-thought reasoning in language models. *arXiv preprint arXiv:2302.00923*, 2023.
- Zhong, Y., Yang, J., Zhang, P., Li, C., Codella, N., Li, L. H., Zhou, L., Dai, X., Yuan, L., Li, Y., et al. Regionclip: Region-based language-image pretraining. In *CVPR*, pp. 16793–16803, 2022.
- Zhou, K., Yang, J., Loy, C. C., and Liu, Z. Conditional prompt learning for vision-language models. In *Proceedings of the IEEE/CVF conference on computer vision and pattern recognition*, pp. 16816–16825, 2022a.
- Zhou, K., Yang, J., Loy, C. C., and Liu, Z. Learning to prompt for vision-language models. *International Journal of Computer Vision*, 130(9):2337–2348, 2022b.
- Zhu, B., Niu, Y., Han, Y., Wu, Y., and Zhang, H. Prompt-aligned gradient for prompt tuning. In *Proceedings of the IEEE/CVF international conference on computer vision*, pp. 15659–15669, 2023.
- Zhu, Y., Zhou, D., Xiao, J., Jiang, X., Chen, X., and Liu, Q. Hypertext: Endowing fasttext with hyperbolic geometry. *arXiv preprint arXiv:2010.16143*, 2020.